Carrier Diffusion Lengths in Hybrid Perovskites: Processing, Composition, Aging and Surface Passivation Effects

Gede W. P. Adhyaksa[†], Leon W. Veldhuizen[‡], Yinghuan Kuang[‡], Sarah Brittman[†], Ruud E. I. Schropp[‡], and Erik C. Garnett[†]*

[†]Center for Nanophotonics, FOM Institute AMOLF, Science Park 104, 1098 XG Amsterdam, The Netherlands

[‡]Department of Applied Physics, Plasma & Materials Processing, Eindhoven University of Technology, P.O. Box 513, 5600 MB Eindhoven, The Netherlands

Supporting Information Placeholder

ABSTRACT: Considering the many possibilities for all three ions in the hybrid halide perovskite structure, hundreds of distinct compositions have already been reported. Such compositional changes can alter the carrier diffusion length - a key parameter for solar cell performance. Given the large compositional and processing parameter space, a rapid and simple technique for directly measuring diffusion length is needed. Here we use a laser grating technique to screen the diffusion length in perovskite materials. First, we control the processing conditions and the resulting grain size to increase the diffusion length in pure $CH_3NH_3PbI_3$. Next, we partially replace iodide with bromide and show that surprisingly, the diffusion length increases after aging for 1 month in air. Finally, we use a 4 nm Al_2O_3 layer to passivate the surface of $CH_3NH_3PbBr_3$, leading to a remarkable increase in diffusion length from 201 nm to 532 nm. The correlation that we have established between material processing and diffusion length offers guidance in how to improve materials for devices.

Hybrid halide perovskites are an emerging class of semiconductors that has drawn great interest recently because of its simple solution processing, tunable band gap, high solar cell efficiency and low lasing threshold.[1-5] They have the same ABX_3 configuration as the classic oxide perovskites but have metal halide rather than metal oxide corner-sharing octahedra. Typically, organic cation A is methylammonium (MA) or formamidinium (FA), B is lead (Pb) or tin (Sn), and X is chloride (Cl), bromide (Br) or iodide (I); already combining just these ions in pure or 50/50 mixes, nearly 50 distinct varieties emerge. Such compositional variations strongly affect material properties. For example, the addition of only a few percent of $PbCl_2$ to $MAPbI_3$ (so-called $MAPbI_{3-x}Cl_x$) increases the film's diffusion length from ~100 nm to ~1 µm and raises optimized photovoltaic efficiency from 4.2% to 12.2%.[6] Even within a single material composition, solvent engineering used to increase the grain size of the film has already been shown to have dramatic effects on device performance.[3,7] While there are many ways to screen materials and processing conditions, the diffusion length of the photo-generated carrier has been one of the properties most strongly correlated with optoelectronic device performance.[6,8] Despite this importance, the most common methods for measuring this diffusion length are not compatible with simple, rapid screening that would be ideal for testing the large number of possible new materials and processing conditions. For example, photoluminescence lifetime measurements can be combined with mobility measurements to yield indirectly the carrier diffusion length, but these measurements are impractically slow to be used for routine testing. Clearly a simple, rapid and direct method for measuring diffusion length would be useful in screening both new hybrid halide perovskite materials and processing conditions that lead to better material quality.

Here we apply such a method, called the steady-state photo carrier grating (SSPG) technique, to hybrid perovskite materials and use it to investigate the influence of material composition, material processing conditions, aging and surface passivation on the diffusion length. Originally developed in the 1980s as a way to measure diffusion length in amorphous silicon thin films, SSPG relies on a change in conductivity in the presence of an optical grating created by two interfering laser beams.[9,10] First, we use SSPG to show that varying the solvent and processing conditions can lead to at least a factor of two variation in the diffusion length of methyl ammonium lead iodide ($MAPbI_3$). Next we demonstrate how the diffusion length varies with halide substitution, and for each composition, how it changes with aging. Finally, we show that a thin (4 nm) passivating aluminum oxide layer can increase the diffusion length of methyl ammonium lead bromide ($MAPbBr_3$) by nearly a factor of three, while the process of adding the same coating dramatically degrades $MAPbI_3$.

Figure 1a shows a schematic of our SSPG measurement setup, where we measure a small change in sample conductivity (at a given voltage) in the presence of an optical grating. The optical grating is created by overlapping two interfering laser beams on the sample. The measurement is conducted under illumination of I_1 and I_2, where the intensity of beam I_1 is much stronger than the chopped beam I_2. In this way, I_1 serves as a background illumination ensuring an almost constant carrier generation rate over the sample surface, while I_2 acts as a probe beam providing a small perturbation (~5%). The change in conductivity is directly measured on the sample

using a lock-in amplifier for two configurations: (1) when the two beams have orthogonal polarization states and therefore do not interfere (Figure 1b), and (2) when the polarization states are aligned, creating a periodic optical grating (Figure 1c). The grating period can be controlled by changing the angle between the two beams (grating period decreases as angle increases). The down-transport mirrors, up-transport mirrors, and the rotating stages enable continuous overlap between I_1 and I_2 with varying angle.

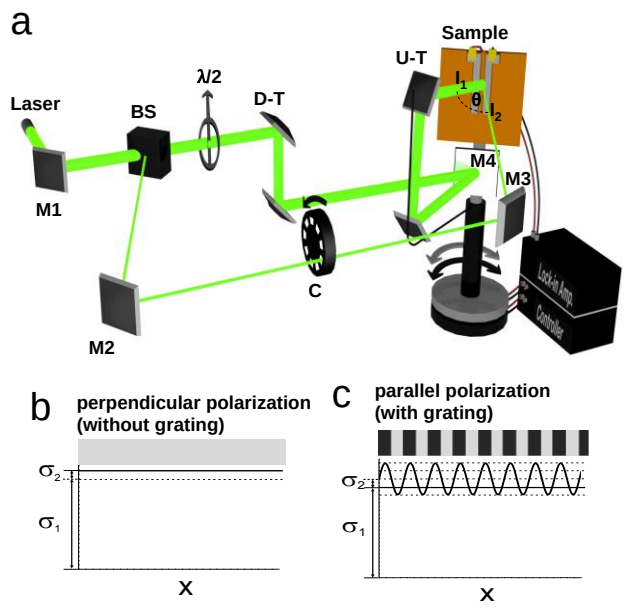

Figure 1. (a) Schematic of the set-up: I_1 is the strong beam, I_2 is the weak beam, θ is the angle between I_1 and I_2, M_1, M_2, M_3, M_4 are mirrors, *BS* is a beam splitter, *λ/2* is a half-wave plate, *C* is a chopper, *U-T* are up-transport mirrors, *D-T* are down-transport mirrors. The axis has two rotating stages (black and gray) and each can rotate independently: (1) the sample along with M_4 underneath (gray arrow) and (2) the up-transport mirrors connected with the arm (black arrow). Sample: a perovskite film deposited on a glass substrate with two co-planar gold electrodes. (b) Lateral conductivity pattern without grating: when I_1 and I_2 are orthogonally polarized. (c) Lateral conductivity with grating: when I_1 and I_2 are in parallel polarization. The conductivity σ_1 and σ_2 are not to scale for better visualization (perturbation by σ_2 should be very small relative to σ_1 in order to maintain the steady-state condition).

Solving the one dimensional steady-state diffusion equation leads to a relation between the photoconductivity ratio and grating period: [11-13]

$$\left(\frac{1}{1-\beta}\right)^{1/2} = \frac{(2\pi L_D)^2}{(2Z)^{1/2}}\left(\frac{1}{\Lambda^2}\right)^2 + \frac{1}{(2Z)^{1/2}} \quad (1)$$

where Λ is the grating period, β is the photoconductivity ratio of lock-in amplifier signals under the parallel and perpendicular polarization configurations (Figure 1c, and 1b), L_D is the diffusion length of the photogenerated carrier and Z is a fitting parameter related to non-ideal grating formation (e.g. due to surface scattering or poor photoconductivity). L_D describes ambipolar transport of the Coulomb-coupled electron and hole, but it will be dominated by the photogenerated carrier with the smaller diffusion length. The value of β will be close to unity when the diffusion length is much longer than the grating period. This case takes place when carrier diffusion significantly smears out the grating, so that the signal is the same if I_1 and I_2 create a grating (Fig. 1c) or not (Fig. 1b). Increasing the grating period beyond the diffusion length drastically decreases the sample conductivity, consequently decreasing β. The value of Z falls between 0 and 1 ($0 < Z < 1$; 1 is for a perfect grating) and depends on factors such as photo-sensitivity of the sample and grating contrast ratio.[10] The diffusion length (L_D) can be directly extracted from a linear fit of equation 1, with error bars coming from the fitting procedure (see SI for details).

This technique measures the change in photoconductivity laterally across the sample, which is associated with the diffusion of photo-generated carriers.[6,8,14] This measurement geometry is distinct as compared to other methods that measure carrier diffusion through the thickness of the film. Although in a standard solar cell, current is extracted in the direction perpendicular to the substrate through the thickness of the film, diffusion in the lateral direction is still strongly correlated to device efficiency for materials whose transport is not strongly anisotropic. For example, a study of halide perovskite thin film devices with grain sizes 100 times larger than the film thickness has shown that grain boundary recombination still plays a role in decreasing solar cell performance, indicating the influence of lateral diffusion.[15] This indicates that the diffusion length measured by SSPG in the lateral geometry is a relevant parameter for solar cell performance. In this work, to confirm that the SSPG technique applied to hybrid perovskites yields a diffusion length similar to that measured by more conventional techniques, we used electron beam induced current (EBIC) to measure the diffusion length of $MAPbI_3$ and $MAPbBr_3$ films of the same quality, processing conditions, and lateral sample geometry used for SSPG measurements. The EBIC values agree well with those obtained using SSPG (Fig. S8). A full description of the technique including theoretical derivation and error analysis for a wide range of thin-film semiconductors, and studies on the effect of laser intensity, electric field, and chopping frequency are the focus of a forthcoming manuscript.

We begin by studying the dependence of diffusion length on sample preparation method using $MAPbI_3$. Samples were prepared by depositing thin-film hybrid perovskites on glass substrates by spin casting from different solvents (details in the supporting information). On top of the film, two gold electrodes were deposited (1 mm spacing) for electrical contacts. Figure 2a shows a transform of the change in conductivity ratio (β) as a function of the grating size (Λ) for $MAPbI_3$ and the corresponding diffusion lengths for each of the three processing conditions. The film processed with dimethylsulfoxide (DMSO) solvent yielded the longest diffusion length (up to 490 nm) followed by the dimethylformamide (DMF, up to 396 nm) and γ-butyrolactone (GBL, up to 288 nm) films. The SEM images show morphological differences consistent with the measured diffusion lengths: films cast from DMSO formed large, smooth plates, while films from DMF were continuous but had a higher roughness, and those cast from GBL had the highest porosity (Figures 2b-d). A variety of different processing treatments including solution filtration before spin coating and toluene anti-solvent dripping also were tested and showed distinct differences in diffusion length

(more detail in Figure S1a). The diffusion length values we measure are similar to what has been reported using other techniques including intensity modulated photocurrent/photovoltage spectroscopy (IMPS/IMVS), photoluminescence quenching and photoluminescence lifetime combined with mobility, where values of 100-1000 nm are typical, depending on preparation conditions.[6,8,14]

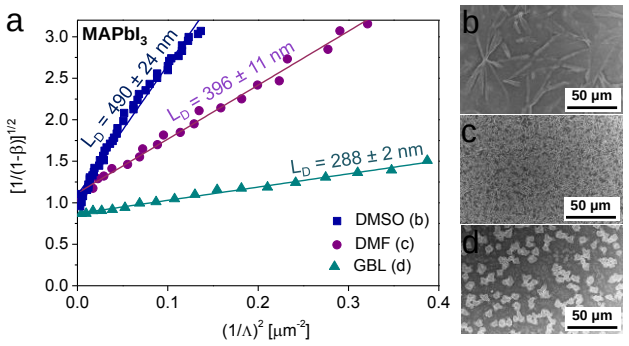

Figure 2. Variation of lateral carrier diffusion length in $MAPbI_3$. (a) Experimental data of a transform of the photoconductivity ratio (β) as a function of grating size (Λ). The lines are the linear fitting of each corresponding experimental dataset. Corresponding scanning electron microscope images of samples prepared with different solvents: (b) DMSO, (c) DMF, (d) GBL.

To gain more insight into the origins of the observed morphology that is created by the solvent, we analyze x-ray diffraction patterns of six $MAPbI_3$ films processed from DMSO, DMF, and GBL, each with two different preparation conditions (Figure S1b). All films show a perovskite structure with a tetragonal phase/P4mm (a = b = 8.86 Å, c = 12.67 Å) typical of literature reports for $MAPbI_3$.[7,16] We observed a direct correlation between diffusion length and the broadening of the XRD peak (Figure S1c-e), which could arise from effects such as smaller crystallite size or micro strain within the film.[17] Assuming that the broadening arises entirely from the size of the crystallites, the full width half maximum of the peak corresponding to the (220) crystal orientation was used to estimate the crystallite size in the six $MAPbI_3$ films with different sample preparation conditions (SI for details). The diffusion length increased by more than a factor of two (from 216 nm to 490 nm) with an increase in estimated crystallite size from 78 nm to 152 nm.

In addition to looking at solvent and preparation effects on diffusion length in the pure iodide, we have also examined how the diffusion length varies with halide composition. Here samples based on neat and mixed $MAPbI_3$ and $MAPbBr_3$ (hereafter denoted as $MAPb(I_{1-x}Br_x)_3$) are studied. The mixed $MAPb(I_{1-x}Br_x)_3$ is of interest because its bandgap can be tuned throughout the region of interest for multi-junction solar cells and visible light-emitting diodes or lasers[2,4,18-22], although there are currently some problems with spontaneous phase separation under solar illumination.[23] We soaked the samples under laser illumination before the SSPG measurement in order to stabilize the properties (see methods). Spin coating from the mixed halide solutions was used to prepare these alloy samples (see methods). The bandgap gradually becomes larger by adding $MAPbBr_3$ into the neat $MAPbI_3$, as can be seen from the gradual blue-shifted absorption with a clear onset following a linear relation: $E_G = 0.69\,[Br] + 1.55$; where E_G is the optical bandgap (eV) and [Br] is the $MAPbBr_3$ fraction relative to $MAPbI_3$; from 0 to 1 (Figure S2a-b). At the same time, there is also a transition from the tetragonal phase to the cubic phase, as shown by the evolution of the tetragonal phase (110) peak into the cubic phase (100) peak, by adding $MAPbBr_3$ into the neat $MAPbI_3$ based on x-ray diffraction analysis[2] (Fig. S2c-d). There is only one single phase observed across the transition from tetragonal to cubic phase implying a successful incorporation of iodide-bromide ions into the perovskite structures.

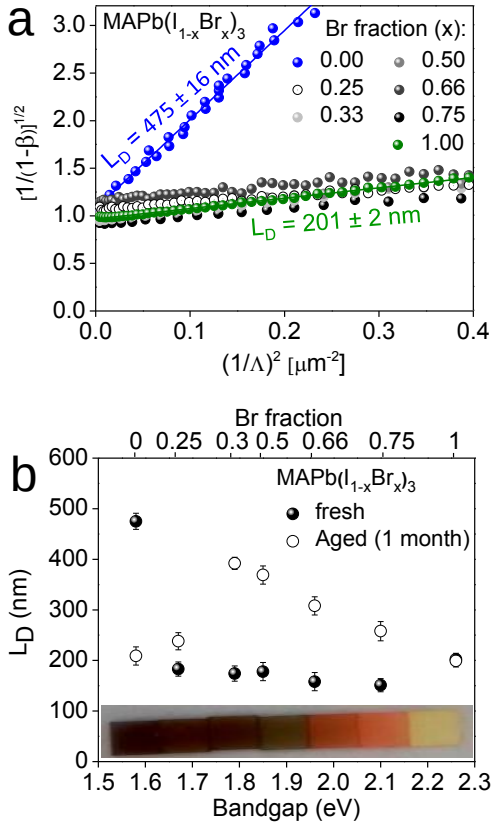

Figure 3. Diffusion length and aging effects in $MAPb(I_{1-x}Br_x)_3$. (a) Experimental data of a transform of the photoconductivity ratio (β) as a function of grating size (Λ) before aging. The lines are the linear fitting of data from each corresponding composition (the fitting lines and diffusion length for mixed samples are not displayed for clarity). (b) Diffusion length as a function of (initial) bandgap and bromide fraction: fresh samples (filled circle), and aged samples (open circle); inset: photograph of aged samples arranged with their corresponding bandgap.

The plot in figure 3a shows that the $MAPbI_3$ film has a diffusion length (475 nm) about two times longer than that of the $MAPbBr_3$ film (201 nm), as indicated by its steeper slope. All alloy compositions initially exhibit diffusion lengths below those of both pure $MAPbBr_3$ and $MAPbI_3$ (Figure 3b), consistent with an earlier proposal of trap-state formation in the mixed halide perovskites.[23] Interestingly, after aging the films for 1 month (stored in air at room temperature in the dark) all mixed halide films show a substantial increase in diffusion length from initial values of 151-183 nm to final values of 238-392 nm (Figure 3b and Figure S3). The diffusion length in

aged alloy films increases proportionally with the Br fraction up to 0.66 (at 1.97 eV band gap) before dropping to values very close to those seen in the pure bromide film. The pure bromide film showed no change in diffusion length with aging, while the pure iodide film showed a large decrease in diffusion length after one month. This result is consistent with the XRD, which showed partial decomposition to lead iodide only for the pure iodide perovskite; the pure bromide and mixed halide perovskite films showed no crystalline secondary phases (Figure S2c). The only change in the alloy perovskite films with aging was a slight blue shift in the absorption onset (Figure S2a-b), consistent with a previous report.[20]

The origin of increased diffusion length with aging for mixed halide perovskite films is still unclear, but reactive oxygen species have been reported to play a role in deactivating defect states in the mixed halide perovskites. [24,25] This strong difference in stability with variation in composition underlines the importance of having a simple and rapid technique for directly measuring the diffusion length of the perovskite itself, isolating its aging characteristics from those of the interfacial and contact layers used in complete devices.

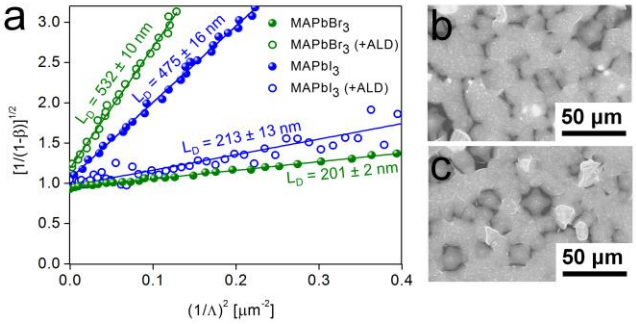

Figure 4. Surface passivation effect on the lateral diffusion length. (a) Experimental data of a transform of the photoconductivity ratio (β) as a function of grating size (Λ) before and after passivation with 4-nm thin aluminum oxide film deposited by atomic layer deposition (ALD); the lines are the linear fitting of each corresponding data. Scanning electron microscope images of MAPbBr3 before (b) and after (c) ALD; the bright-small dots are from sputtered chromium particles.

Although the experiment creates an optical grating throughout the entire perovskite film thickness, a transfer-matrix calculation[26,27] shows that the highest photocarrier generation rate occurs at the surface of the film (Figure S5). This suggests that the SSPG technique could be sensitive to surface recombination and surface passivation effects.[28] Figure 4 shows the transform of the photoconductivity ratio as a function of grating size of $MAPbI_3$ and $MAPbBr_3$ films before and after coating with a 4-nm thin amorphous aluminum oxide (Al_2O_3) layer deposited by atomic layer deposition (ALD). The deposition takes place at 100°C using trimethylaluminum (TMA) and water (H_2O) as the Al_2O_3 precursors and the whole process takes 30 minutes (50 cycles). There is a dramatic increase in diffusion length for the $MAPbBr_3$ film from 201 nm to 532 nm, while the diffusion length of the $MAPbI_3$ film decreases from 475 nm to 213 nm. From XRD it is clear that $MAPbI_3$ decomposes substantially, as indicated by the appearance of PbI_2 precursor peaks (Figure S6) after the ALD deposition. In fact, we observed that the $MAPbI_3$ had started to decompose even after 10 cycles of ALD (<1 nm). This can explain both the lower diffusion length and poor signal to noise ratio in the measurement. In contrast, the cubic phase of $MAPbBr_3$ is still preserved without any trace of precursor peaks observed (Figure S6).

To elucidate if surface passivation is the main reason for the diffusion length improvement, we conducted a vacuum annealing experiment by placing a $MAPbBr_3$ film in the ALD chamber in which all parameters were set to be the same (100°C, 30 minutes, 10^{-3} mbar), only without feeding in the precursors. We observed the diffusion length also increased after the vacuum annealing, but only by about 20% from its initial value, which cannot account for the nearly three-fold increase seen after ALD (Figure S7). Previously a thin ALD alumina layer has been shown to be an effective passivation scheme for a variety of semiconductor surfaces (Si[29], CIGS[30], ZnO[31]) either through a field effect (fixed interfacial charges) or reduced interfacial trap state density, both of which reduce the surface recombination velocity. However, the exact role of the ALD passivation on hybrid perovskites is still under investigation. As ALD has been used in the past as an encapsulation layer to improve the stability of metal nanowire transparent electrodes[32], we expect it could also serve a similar role here.

To summarize, we have performed a simple and rapid technique to screen quantitatively the diffusion length in hybrid perovskite thin films. This laser grating technique directly measures the diffusion length, which eliminates the need to measure lifetime and mobility separately. We demonstrate that the diffusion length in $MAPbI_3$ films can be improved from 216 nm to 490 nm by changing the deposition conditions. We also show that the diffusion length in mixed $MAPb(I_{1-x}Br_x)_3$ films has a complex aging behavior that varies dramatically with composition: pure iodide films degrade, pure bromide films do not change and the alloy films improve with aging. Finally, we demonstrate an improvement in the diffusion length of $MAPbBr_3$ films from 201 nm to 532 nm after deposition of a 4-nm thin Al_2O_3 layer by ALD. This remarkable improvement in diffusion length justifies further investigations on interfacial modification with other oxides such as nickel oxide (NiO_x), molybdenum oxide (MoO_x), and titanium oxide (TiO_x) for broadening its applicability not only for solar cells but also for photo-electrochemical water splitting.

Supporting Information

Sample preparation, atomic layer deposition, laser grating setup, x-ray diffraction, transfer matrix modelling, error analysis, electron beam induced current measurements, and data analysis. This material is available free of charge via the Internet at http://pubs.acs.org.

AUTHOR INFORMATION

Corresponding Author

*e.garnett@amolf.nl

Notes

The authors declare no competing financial interests.

ACKNOWLEDGMENT

The authors thank Dr. Bruno Ehrler for comments on the manuscript, Haralds Abolins for discussion and suggestions for thin film deposition protocols, Dibyashree Koushik for cross-checking the XRD data, Andries Lof, Parisa Khoram, and Dr. Sophie Meuret for help and discussions regarding the EBIC measurements, and Ricardo Struik for the schematic drawn in Figure 1a. This work is part of the research program of the Foundation for Fundamental Research on Matter (FOM), which is part of the Netherlands Organization for Scientific Research (NWO). L.W. Veldhuizen, and R. E. I. Schropp acknowledge NanonextNL (project 02A.03), a micro and nanotechnology consortium of the government of the Netherlands and 130 partners. G.W.P. Adhyaksa, S. Brittman, and E.C. Garnett acknowledge financial support from the European Research Council under the European Union's Seventh Framework Programme (FP/2007-2013)/ERC Grant Agreement no. 337328, "NanoEnabledPV," and from an industrial partnership between Philips and FOM.

REFERENCES

(1) Lee, M. M.; Teuscher, J.; Miyasaka, T.; Murakami, T. N.; Snaith, H. J. Efficient hybrid solar cells based on meso-superstructured organometal halide perovskites. *Science* **2012**, *338*, 643-647.

(2) Noh, J. H.; Im, S. H.; Hoe, J. H.; Mandal, T. N.; Seok, S. I. Chemical management for colorful, efficient, and stable inorganic-organic hybrid nanostructured solar cells. *Nano Lett.* **2013**, *13*, 1764–1769.

(3) Jeon, N. J.; Noh. J. H.; Yang, W. S.; Kim, Y. C.; Ryu, S.; Seo, J.; Seok, S. I. Compositional engineering of perovskite materials for high-performance solar cells. *Nature* **2015**, *517*, 476-480.

(4) Zhu, H.; Fu, Y.; Meng, F.; Wu, X.; Gong, Z.; Ding, Q.; Gustafsson, M. V.; Trinh, M. T. ; Jin, S.; Zhu, X-Y. Lead halide perovskite nanowire lasers with low lasing thresholds and high quality factors. *Nat. Materials* **2015**, *14*, 638-642.

(5) Burschka, J.; Pellet, N.; Moon, S-J.; H-Baker, R.; Gao, P.; Nazeeruddin, M. K.; Gratzel, M. Sequential deposition as a route to high-performance perovskite-sensitized solar cells. *Nature* **2015**, *499*, 316-319.

(6) Stranks, S. D.; Eperon, G. E.; Grancini, G. ; Menelaou, C. ; Alcocer, M.J.P.; Leijtens, T.; Herz, L. M.; Petrozza, A.; Snaith, H. J. Electron-hole diffusion lengths exceeding 1 micrometer in an organometal trihalide perovskite absorber. *Science* **2013**, *342*, 341-344.

(7) Jeon, N.J.; Noh, J. H.; Kim, Y. C.; Yang, W. S.; Ryu, S.; Seok, S. I. Solvent engineering for high-performance inorganic-organic hybrid perovskite solar cells. *Nat. Materials* **2014**, *13*, 897-903.

(8) Xing, G.; Mathews, N.; Sun, S.; Lim, S. S.; Lam, Y. M.; Gratzel, M.; Mhaisalkar, S.; Sum, T. C. Long-range balanced electron-and hole-transport lengths in organic-inorganic $CH_3NH_3PbI_3$. *Science* **2013**, *342*, 344-347.

(9) Komoro, S.; Aoyagi, Y.; Segawa, Y.; Namba, S.; Masuyama, A.; Okamoto, H.; Hamakawa, Y. Study of optically induced degradation of conductivity in hydrogeneted amorphous silicon by transient grating method. *App. Phys. Lett*. **1983**, *42*, 807-809.

(10) Ritter, D.; Zeldov, E.; Weiser, K. Steady-state photocarrier grating technique for diffusion length measurement in photoconductive insulators. *App. Phys. Lett*. **1986**, *49*, 791-793.

(11) Balberg, I.; Delahoy, A. E.; Weakliem, H. A. Self-consistency and self-sufficiency of the photocarrier grating technique. *App. Phys. Let*. **1988**, *53*, 992-994.

(12) Nicholson, J.P. Fresnel corrections to measurements of ambipolar diffusion length. *J. App. Phys*. **2000**, *88*, 4693-4696.

(13) Hattori, K.; Okamoto, H.; Hamakawa, Y. Theory of the steady-state-photocarrier-grating technique for obtaining accurate diffusion-length measurements in amorphous silicon. *Phys. Rev. B.* **1992**, *45*, 1126-1138.

(14) Hoe, J. H.; Song, D. H.; Han, H. J.; Kim, S. Y.; Kim, D.; Kim, H.; Shin, T. K.; Ahn, T. K.; Wolf, C.; Lee, T-W.; Im, S. H. Planar $CH_3NH_3PbI_3$ Perovskite Solar Cells with Constant 17.2% Average Power Conversion Efficiency Irrespective of the Scan Rate. *Adv. Mat*. **2015**, *27*, 3424–3430.

(15) Yang, Y.; Yan, Y.; Yang, M.; Choi, S.; Zhu, K.; Luther, J. M.; Beard, M. C. Low surface recombination velocity in solution-grown $CH_3NH_3PbBr_3$ perovskite single crystal. *Nat. Commun*. **2015**, *6*, 1-6.

(16) Quarti, C.; Mosconi, E.; Ball, J. M.; D'Innocenzo, V.; Tao, C. Pathak, S.; Snaith, H. J.; Petrozza, A.; Angelis, F. D. Structural and optical properties of methylamaonium lead iodide across the tetragonal to cubic phase transition: implications for perovskite solar cells. *Energy Environ. Sci*. **2016**, *9*, 155-163.

(17) Suryanarayana, C.; Norton, M. G. *X-ray diffraction: a practical approach*, Plenum Press, New York, 1998.

(18) White, T. P.; Lal, N. N.; Catchpole, K. R. Tandem solar cells based on high-efficiency c-Si bottom cells: top cell requirements for > 30% efficiency. *IEEE J. Photovolt*. **2014**, *4*, 1-7.

(19) G-Escrig, L.; M.-Sempere, A.; Sessolo, M.; Bolink, H. J. Mixed iodide-bromide methylammonium lead perovskite-based diodes for light emission and photovoltaics. *J. Phys. Chem. Lett*. **2015**, *6*, 3743-3748.

(20) Sadhanala, A.; Deschler, F.; Thomas, T. H.; Dutton, S. E.; Goedel, K. C.; Hanusch, F. C.; Lai, M. L.; Steiner, U.; Bein, T.; Docampo, P.; Cahen, D.; Friend, R. H. Preparation of single-phase films of $CH_3NH_3Pb(I_{1-x}Br_x)_3$ with sharp optical band edges. *J. Phy. Chem. Lett.* **2014**, *5*, 2501-2505.

(21) Kulkarni, S. A.; Baikie, T.; Boix, P. P.; Yantara, N.; Mathews, N.; Mhaisalkar, S. Band-gap tuning of lead halide perovskites using a sequential deposition process. *J. Mat. Chem. A* **2015**, *9*, 9221-9225.

(22) Cho, H.; Jeon, S.-H.; Park, M-H.; Kim, Y-H.; Wolf, C.; Lee, C-L.; Hoe, J. H.; Sadhanala, A.; Myoung, N.; Yoo, S.; Im, S. H.; Friend, R. H.; Lee, T-W. Overcoming the electroluminescence efficiency limitations of perovskite light-emitting diodes. *Science* **2015**, *350*, 1222-1225.

(23) Hoke, E.T.; Slotcavage, D. J.; Dohner, E. R.; Bowring, A. R.; Karunadasa, H. I.; McGehee, M. D. Reversible photo-induced trap formation in mixed-halide hybrid perovskites for photovoltaics. *Chem. Sci*. **2015**, *6*, 613-617.

(24) Tian, Y.; Peter, M.; Unger, E.; Abdellah, M.; Zheng, K.; Pullerits, T.; Yartsev, A.; Sundstrom, V.; Scheblykin, I. G. Mechanistic insights into perovskite photoluminescence enhancement: Light curing with oxygen can boost yield thousandfold. *Phys.Chem.Chem. Phys*., **2015**, *17*, 24978-24987.

(25) Galisteo-Lopez, J. F.; Anaya, M.; Calvo, M. E.; Miguez, H. Environmental effects on the photophysics of organic-inorganic halide perovskites. *J.Phys.Chem. Lett*., **2015**, *6*, 2200-2205.

(26) Peumans, P.; Yakimov, A.; Forrest, S. R. Small molecular weight organic thin-film photodetectors and solar cells. *J. App. Phys.* **2003**, *93*, 3693-3723.

(27) Burkhard, G. F.; Hoke, E. T.; McGehee, M. D. Accounting for intergerence, scattering, and electrode absorption to make accurate internal quantum efficiency measurement in organic and other thin solar cells. *Adv. Mat*. **2010**, *22*, 3293–3297.

(28) Haridim, M.; Weiser, K.; Mell, H. Use of the steady-state photocarrier-grating technique for the study of the surface recombination velocity of photocarriers and the homogeneity of hydrogenated amorphous silicon films. *Philos. Mag. B.* **1993**, *67*, 171-180.

(29) Kato, S.; Kurokawa, Y.; Miyajima, S.; Watanabe, Y.; Yamada, A.; Ohta, Y.; Niwa, Y.; Hirota, M. Improvement of carrier diffusion length in silicon nanowire arrays using atomic layer deposition. *Nanoscale Res. Lett*. **2013**, *8*, 1-8.

(30) Vermang, B.; Fjallstrom, V.; Gao, X.; Edoff, M. Improved rear surface passivation of Cu(In,Ga)Se2 solar cells: a combination of an Al_2O_3 rear surface passivation layer and nanosized local rear point contacts. *IEEE J. Photovolt.* **2014**, *4*, 1-7.

(31) Law, M.; Greene, L. E.; Radenovic, A.; Kuykendall, T.; Liphardt, J.; Yang, P. ZnO-Al2O3 and ZnO-TiO2 core-shell nanowire dye-sensitized solar cells. *J. Phys. Chem. B.* **2006**, *110*, 486-492.

(32) Hsu, P-C.; Wu, H.; Carney, T.J.; McDowell, M.T.; Yang, Y.; Garnett, E. C.; Li, M.; Hu, L.; Cui. Y. Passivation coating on electrospun copper nanofibers for stable transparent electrodes. *ACS Nano* **2012**, *6*, 5150-5156.

TOC

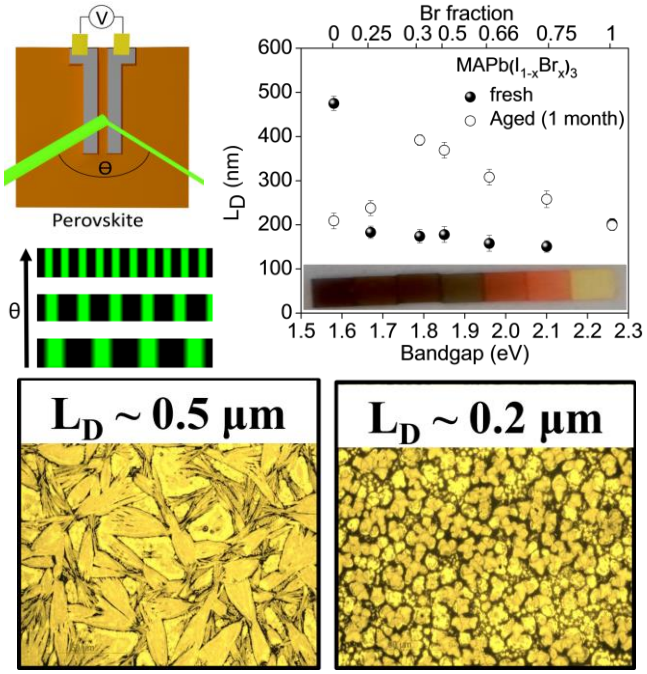
V
θ
Perovskite
θ
Br fraction
0 0.25 0.3 0.5 0.66 0.75 1
MAPb(I1-xBrx)3
fresh
Aged (1 month)
LD (nm)
600
500
400
300
200
100
0
1.5 1.6 1.7 1.8 1.9 2.0 2.1 2.2 2.3
Bandgap (eV)
LD ~ 0.5 µm
LD ~ 0.2 µm

Supporting Information

Carrier Diffusion Lengths in Hybrid Perovskites: Processing, Composition, Aging and Surface Passivation Effects

Gede W. P. Adhyaksa[†], Leon W. Veldhuizen[‡], Yinghuan Kuang[‡], Sarah Brittman[†], Ruud E. I. Schropp[‡], and Erik C. Garnett[†]*

[†]Center for Nanophotonics, FOM Institute AMOLF, Science Park 104, 1098 XG Amsterdam, The Netherlands

[‡]Department of Applied Physics, Plasma & Materials Processing, Eindhoven University of Technology, P.O. Box 513, 5600 MB Eindhoven, The Netherlands

*e.garnett@amolf.nl

Experimental protocol and Characterization

Sample preparation:

Perovskite films were deposited on insulating glass substrates (1.5 × 1.5 cm). Prior to the deposition, the substrates were cleaned by the following protocol: 15 minutes in acetone (ultra-sonication), 15 min in isopropanol (ultra-sonication), 1-2 hours under hydrochloric acid bath (18 % in deionized water); between each step the substrates were rinsed with isopropanol and dried with nitrogen (N_2) flow; the substrates were then cleaned using an oxygen plasma (50 W, 2 mins) to make the surface hydrophilic. The perovskite film was formed by spin-coating (10,000 rpm, for 60 seconds) a perovskite solution (1-2M in DMSO, 1M DMF, or 1M GBL) on the glass substrate followed by thermal annealing at 100°C for 30 minutes; all deposition processes were conducted in a N_2 glovebox. The perovskite solutions were prepared following the previous report.[1] It was synthesized by mixing equimolar concentrations of methylammonium halides (CH_3NH_3X; X = I, Br) and lead halide (PbX_2; X = I, Br) precursors. The mixture was ultra-sonicated to help dissolving any precursor flakes followed by 2-3 hours stirring in the N_2 glove box. The CH_3NH_3X was synthesized by mixing methylamine (Sigma-Aldrich, 33 wt. % in ethanol) and hydrobromic (or hydroiodic) acid (Sigma-Aldrich, 48-57% in H_2O) in an ice bath for 2 hours. The solvents were evaporated by heating the solution at 150°C while stirring until a white or occasionally yellowish powder was formed. The powder was then recrystallized from a boiling ethanol to form white powders (CH_3NH_3I) or flakes (CH_3NH_3Br). The PbI_2 and $PbBr_2$ were used as purchased (Sigma-Aldrich, 99%). For mixed $CH_3NH_3Pb(I_{1-x}Br_x)_3$ solution, 1M $CH_3NH_3PbI_3$ solution and 1M $CH_3NH_3PbBr_3$ solutions were mixed by varying the volume ratio (for example 1:3 of I:Br means 1mL of 1M $CH_3NH_3PbI_3$ mixed with 3mL of 1M $CH_3NH_3PbBr_3$). Two co-planar gold electrodes were deposited on the thin film perovskites using a thermal evaporator (base pressure 10^{-5} mbar). The thickness of the electrodes was ~100-170 nm with 1 mm spacing in between. For the optimized condition: the optimized films with DMSO or GBL were from 1M filtered solution of $MAPbI_3$ (0.22 micron, PTFE), and the solution was stirred overnight at 60°-70°C before the deposition. Optimized films with DMF were from 2M solution of $MAPbI_3$, hydrochloric iodic was added into the solution (< 8% v/v), toluene drop casting during the spin-coating (at 10^{th}-15^{th} second out of 60 seconds spinning). Otherwise, non-optimized films are from 1M solution of $MAPbI_3$ with 60 seconds spinning with no pre-heat treatment of solution involved.

Atomic layer deposition (ALD):

Al_2O_3 was deposited on the thin film of hybrid perovskites in an Oxford Instrument OpAL™ reactor. The 4-nm Al_2O_3 layer, with thickness monitored by an *in situ* spectroscopic ellipsometry, were deposited on the substrate by 50 cycles at 100°C. Each ALD cycle consists

of an $Al(CH_3)_3$ dosing of 0.02 s, followed by a purge of 3.5 s, then a water vapor exposure of 0.02 s, followed by a purge of 3.5 s.

Laser grating setup:
A diode-pumped solid-state laser (532 nm, LasNova Series 50 green) was used as an excitation source. The power output, coherence length, and polarization ratio of the laser was 4.1 mW, > 5cm, and 500:1, respectively. The beam was split into two-coherent beams at a BK7 glass window. The intensity ratio I_1/I_2 between the two beams was 15, and adjusted by a neutral density filter. A DC voltage of 10 V was applied via the two electrodes on the sample, corresponding to an electric field strength of about 100 V/cm. This field strength was low enough to be in the diffusion regime. The polarization of beam I_1 was changed by a half-wave plate. The beam I_2 was chopped at 110 Hz. Two rotatable mirrors were used to direct the two beams onto the sample aiming for continuous overlap while changing the angle between the two-interfering beams. For hybrid perovskite measurements, to be in the linear regime, we typically varied the angle from 3° to 15°, and this corresponds to optical grating periods from ~5 microns down to ~0.8 microns; the lower boundary for the measured diffusion length is about 0.1 times the grating period. The sample was pre-soaked under ~100 mW/cm^2 laser illumination for 1-2 minutes before the measurement to minimize the light-induced phase separation effect to ensure consistent measurements.

X-ray diffraction (XRD):
The crystal structure of the samples was analyzed based on their x-ray diffraction spectra (using a Bruker D2-phaser instrument, Bragg-Brentano geometry) under the *θ-2θ* configuration. The average crystallite size was determined using the Scherrer equation[2]:

$$< \mathrm{R} > = \frac{\mathrm{k}\lambda}{\mathrm{B}\cos\theta} \qquad (2)$$

Where <*R*> is the average crystallite size in the crystal direction along the normal of the diffraction plane, *k* is a constant that depends on the crystallite shape, but normally is approximately 0.94 (*k* = 0.94 for a cubic crystallite shape), λ is the x-ray wavelength (here, λ = 0.154 nm for *Cu-Kα*), *B* is the *2θ* full width half maximum (FWHM) peak (in radian) after correction by the FWHM contributed by the instrumental broadening, θ is the Bragg angle. The FWHM correction was done by taking the XRD spectra of a certified Corundum standard and subtracting the XRD FWHM peak of the perovskite at 28.8° (220) with the Corundum FWHM peak at 25.6°. A systematic error due to a different sample thickness (*Z*-height error correction) is minimized by scanning XRD spectra of a sample also containing CeO_2, and then adjusting the peak position according to the pure CeO_2 standard. The error range of <*R*> for each sample was estimated by calculating the <*R*> on 3-4 samples with the same preparation condition. All measurements were performed under the same instrumental setting: using 0.6 mm divergence slit to control illuminated area, 1 mm beam knife to limit unwanted scattering and optimize the low angle spectra, nickel filter to reduce 20-30% contribution from *Cu-Kβ*. The scan interval ($\Delta 2\theta$) was 0.01° with multiple scans repeated to improve signal to noise ratio.

Scanning electron microscope (SEM):
The SEM images of the samples were taken after the diffusion length measurement with a 2-nm sputtered chromium deposited on the samples. A through lens detector (TLD) for secondary electrons (SEM, FEI Verios 460) was used to scan the top-view morphology across the sample. The images were recorded using an accelerating voltage of 10 kV.

Electron beam induced current (EBIC):
The samples for the EBIC measurement were prepared by depositing hybrid perovskite films on metal electrodes. Gold (Au) and titanium (Ti) fingers with 2 micron spacing between them were fabricated using two steps of photolithography. The procedure of thin film deposition was the same as that used to prepare the films for the optical grating measurement (see sample preparation protocol). The contacts were wire-bonded to a printed circuit board, allowing the current of the perovskite films to be measured inside the SEM. The EBIC measurement was performed in the same SEM as used for imaging, equipped with a current amplifier (FEMTO, DLPCA-200, gain set to ~10^{11} - 10^{9} V/A), and the electron beam was set at 10 kV, 50 pA, 1 ms integration time. To simulate the electron trajectory for the given electron beam parameters entering our structure, we used a Monte Carlo simulation of the electron's trajectory (CASINO) in the solid with 10^{6} simulated electrons.[7] To extract the photocurrent decay curves, the periodic noise from the EBIC maps was removed by filtering the image in Fourier space, and the current decay profiles over a uniform region of the image were averaged. For the $MAPbI_3$ EBIC images, this region was typically the whole frame, while for the $MAPbBr_3$ EBIC images, smaller areas were used because of non-uniformity in the morphology of the film and charging effects.

Transfer matrix modelling
The 1 dimensional profile of electric field distribution, charge generation, absorption, and reflectance in our sample configuration was modelled using the transfer matrix formalism.[3,4] The electric field profile was calculated for the wavelengths at 532 nm (at laser excitation wavelength) which is just slightly shorter than the absorption edge wavelength of $MAPbBr_3$. The *n-k* values were acquired using diffraction-limited reflection and transmission spectroscopy to determine the local complex refractive index of $MAPbBr_3$ from 400-1100 nm.[5] The *n-k* values for ALD Al_2O_3 were acquired using spectroscopic ellipsometry measurement and interpolated with a cubic spline function. The thickness for the Al_2O_3 was set to be 4 nm, while varying the thickness of $MAPbBr_3$: 250 nm, 500 nm, 1 microns, and 2 microns.

Error analysis
All error bars shown in this report are derived from the linear fitting of the data to the Balberg equation[6]:

$$\text{Balberg equation: } \left[\left(\frac{1}{1-\beta}\right)^{1/2}\right] = \frac{(2\pi L_D)^2}{(2Z)^{1/2}}\left[\left(\frac{1}{\Lambda^2}\right)\right] + \frac{1}{(2Z)^{1/2}} \quad \text{(S1)}$$

$$\text{Linear fitting: } [Y] = a[X] + c \quad \text{(S2)}$$

a is the slope, and c is the intercept. By combining (S1) and (S2), we can calculate the diffusion length as:

$$L_D = \frac{1}{2\pi}\left(\frac{a}{c}\right)^{1/2} \quad \text{(S3)}$$

The error bar of L_D is calculated by summing the error propagation of the slope (a) and the intercept (c):

$$\delta L_D = \frac{1}{4\pi}\left(\frac{a}{c}\right)^{1/2}\sqrt{\left(\frac{\delta a}{a}\right)^2 + \left(\frac{\delta c}{c}\right)^2} \quad \text{(S4)}$$

The δa and δc are errors based on confidence intervals on a and c. The standard error values of a and c from the regression analysis are used to construct δa and δc. Here we take 90% critical values from the t-distribution with 20 to 30 degrees of freedom. This gives 90% confidence intervals that are 1.31 to 1.33 times larger than the standard error values.

EBIC analysis

To validate our SSPG measurements, we compared the diffusion lengths determined using the SSPG technique to diffusion lengths measured using EBIC, which is a well-established technique that also measures lateral diffusion length. EBIC measurements, however, measure only local diffusion length (nm to µm scale), while the SSPG measurements average over the entire film (mm scale).

According to our EBIC measurements, the diffusion lengths obtained from the current decay profiles in $MAPbI_3$ are 555 nm (figure S8e), 512 nm, 537 nm, 454 nm, 518 nm, and 371 nm, as compared to the 490 ± 24 nm measured by the SSPG technique. This range of extracted diffusion length values likely originates from a local difference in crystallinity and film morphology. For the $MAPbBr_3$ film, EBIC-measured diffusion lengths included 215 nm (Figure 8f-h), 164 nm, 219 nm, 128 nm, 172 nm, 186 nm, and 318 nm, as compared to 201 ± 2 nm measured using SSPG. The average values (491 nm and 200 nm for $MAPbI_3$ and $MAPbBr_3$, respectively) are remarkably similar to the SSPG results (490 nm and 201 nm for $MAPbI_3$ and $MAPbBr_3$, respectively). For EBIC, the standard deviation is much larger (62 nm and 56 nm for $MAPbI_3$, and $MAPbBr_3$, respectively), as expected, because of the more local nature of the EBIC measurement. Since EBIC is a well-established technique, these measurements confirm that SSPG provides an accurate measurement of the film's lateral diffusion length averaged over a large scale.

In our EBIC measurements, we needed a relatively high voltage (10 kV) and current (50 pA) to measure a clear EBIC signal. This voltage ensures that the electron beam penetration depth is sufficient for the back electrodes can collect the signal (Fig. S8b). We are aware that others have advocated using a lower voltage (1-3 kV) to prevent film damage over time for hybrid perovskites,[8] but we did not see visible damage to our films with repeated scans. The instability reported in the literature could arise from the film's being damaged by preparing the cross section or from the use of transporting layers (e.g. Spiro-OMeTAD) in the device. In our case, to give a structure comparable to that used for the SSPG measurements, we did not use any transporting layer, relying on the barrier between the metal contact and the perovskite to produce a Schottky contact at which to measure the photocurrent's decay.

1. Noh, J. H.; Im, S. H.; Hoe, J. H.; Mandal, T. N.; Seok, S. I. Chemical management for colorful, efficient, and stable inorganic-organic hybrid nanostructured solar cells. *Nano Lett.* **2013**, *13*, 1764-1769.
2. Suryanarayana, C.; Norton, M. G. *X-ray diffraction: a practical approach*, Plenum Press, New York, USA, **1998**.
3. Burkhard, G. F.; Hoke, E. T.; McGehee, M. D. Accounting for interference, scattering, and electrode absorption to make accurate internal quantum efficiency measurements in organic and other thin solar cells. *Adv. Mat.* **2010**, *22*, 3293-3297.
4. Peumans, P.; Yakimov, A.; Forrest, S. R. Small molecular weight organic thin-film photodetectors and solar cells. *J. App. Phys.* **2003**, *93*, 3693-3723.

5. Brittman, S.; Garnett, E. C. Measuring n and k at the Microscale in Single Crystals of CH3NH3PbBr3 Perovskite. *J. Phys. Chem. C* **2016**, *120*, 616-620.
6. Balberg, I.; Delahoy, A. E.; Weakliem, H. A. Ambipolar diffusion length measurements on hydrogenated amorphous silicon p‐i‐n structures. *App. Phys. Let.* **1988**, *53*, 1949-1951.
7. Demers, H.; N. Poirier-Demers, N.; Couture, AR.; Joly, D.; Guilmain, M.; de Jonge, N.; Drouin, D.; Three-dimensional electron microscopy simulation with the CASINO Monte Carlo software. *Scanning* **2011**, *33*, 92-101.
8. Yuan, H.; Debroye, E.; Janssen, K.; Naiki, H.; Steuwe, C.; Lu, G.; Moris, M.; Origiu, E.; Uji-i, H.; Schryver, F.D.; Samori, P.; Hofkens, J.; Roeffaers, M.; Degradation of methylammonium lead iodide perovskite structures through light and electron beam driven ion migration. *J. Phys. Chem. Lett*. **2016**, *7*, 561–566.

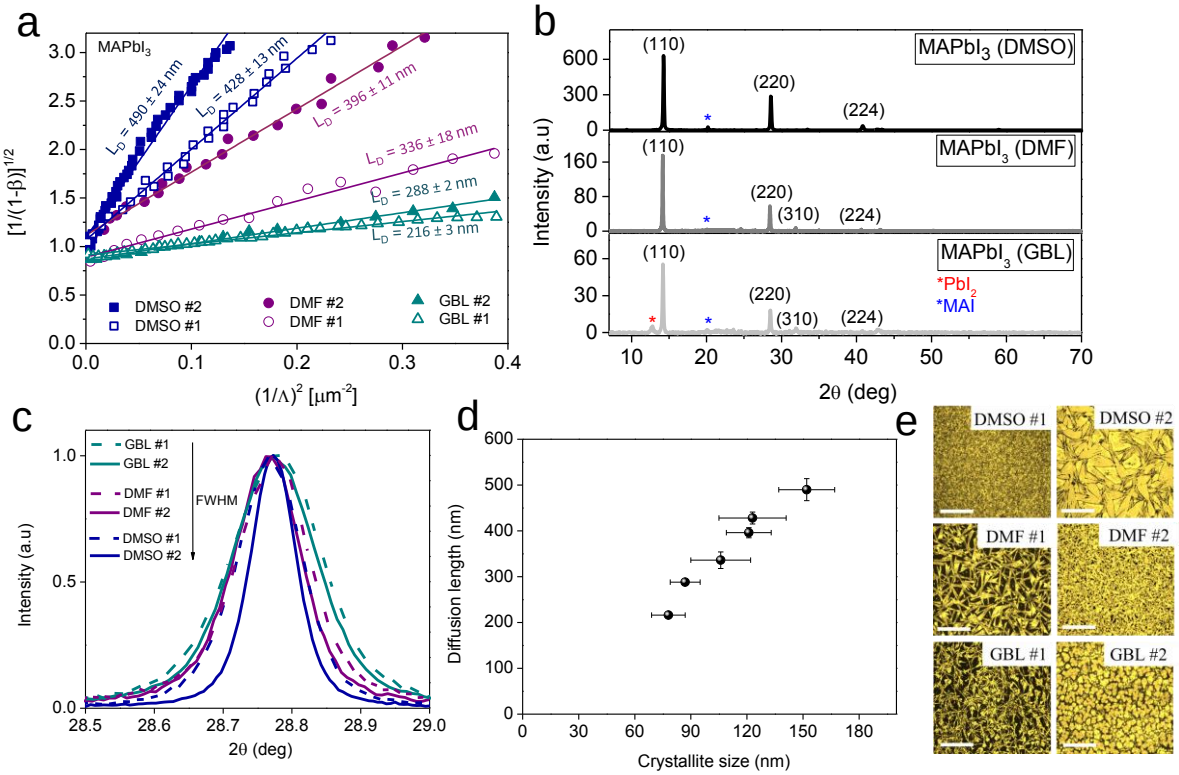

Figure S1. Diffusion length and crystallite size correlation in $MAPbI_3$: (a) Experimental data of a transform of the conductivity ratio (β) as a function of grating size (Λ): The lines are the linear fitting of each corresponding experimental data. (b) XRD spectra scanned from 7-70° and all showing the same crystal phase (tetragonal phase/P4mm (a = b = 8.86 Å, c = 12.67 Å) with small fraction of precursor traces (PbI_2 and MAI). (c) XRD at (220) crystal orientation showing different XRD peak width. (d) Measured diffusion length as a function of estimated crystallite size (determined from the XRD peak width). (e) Optical images (top view, with the scale bar of 50 μm) of samples prepared with different solvent and treatments: #1 refers to non-optimized samples, and #2 refers to the optimized ones.

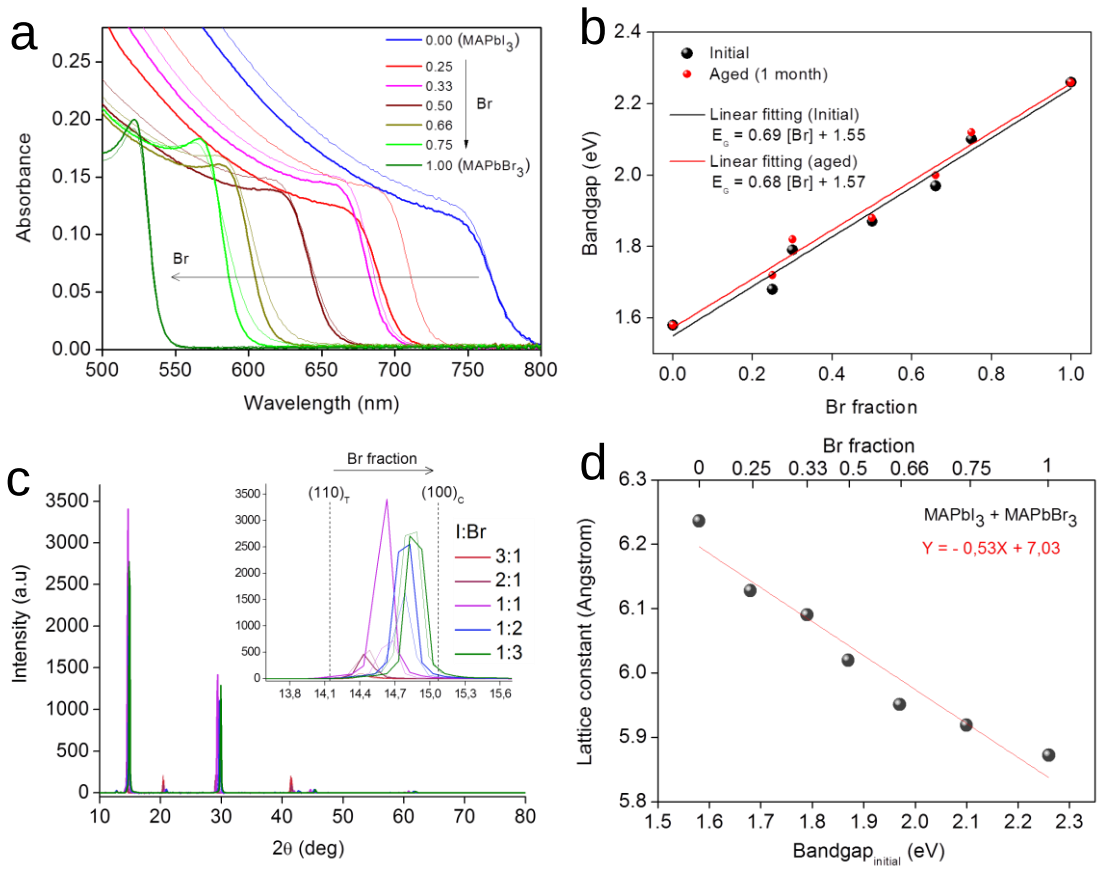

Figure S2. Bandgap and lattice constant correlation in $MAPbI_{3-x}Br_x$: (a) Absorption spectra as a function of wavelength showing a gradual blue-shift for increasing Br fraction before (thin lines) and after (thick lines) 1 month aging in air. (b) Linear correlation of bandgap as a function of Br fraction (bandgap increases with increasing Br fraction) showing the optical stability of $MAPbI_{3-x}Br_x$ after aging for 1 month in air. (c) XRD spectra showing gradual transition from (110) tetragonal to (100) cubic with increasing Br fraction. (d) Linear correlation of lattice constant (derived from the XRD peak) as a function of bandgap showing a linear reduction of lattice constant as the bandgap increases (as Br fraction increases).

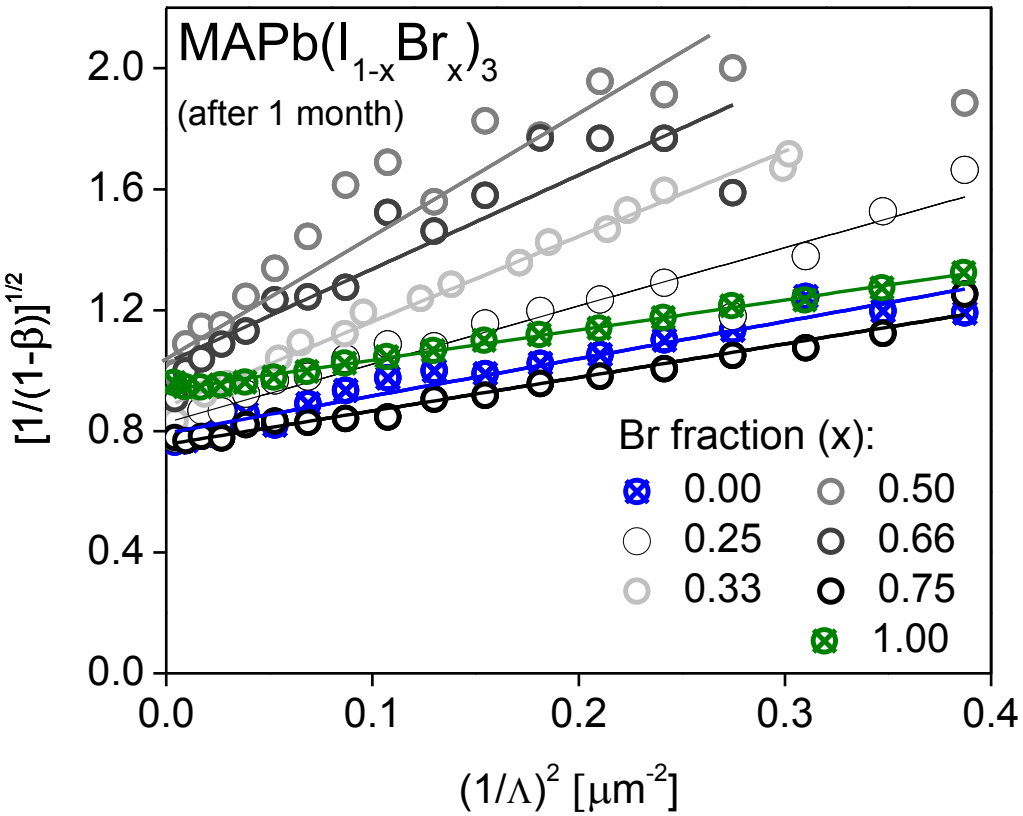

Figure S3. Experimental data of $MAPb(I_{1-x}Br_x)_3$ after 1 month aging (in air): Experimental data of a transform of the conductivity ratio (β) as a function of grating size (Λ), the lines are linear fittings of each corresponding experimental data. Diffusion length values and errors are tabulated in Table S1. The optical images of these samples are in Figure S4.

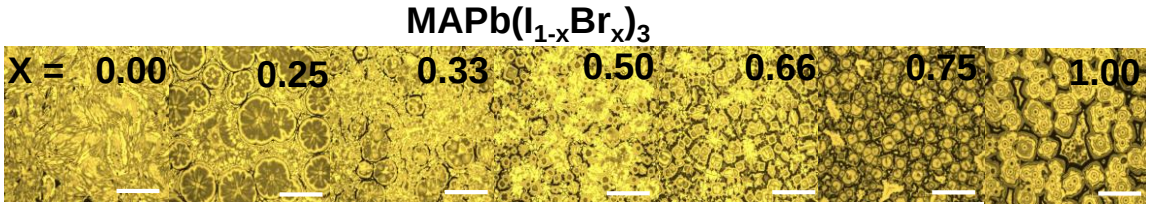

Figure S4. Optical images of $MAPb(I_{1-x}Br_x)_3$ after 1 month aging (in air).

Table S1. Diffusion length values and errors extracted from figure S3a.

Br fraction	Bandgap (eV)	Fresh		Aged (1 month)	
		L_D (nm)	Error L_D (nm)	L_D (nm)	Error L_D (nm)
0	1.58	475	16	209	18
0.25	1.67	183	14	238	17
0.30	1.79	174	15	392	12
0.50	1.85	178	18	369	18
0.66	1.96	158	18	308	18
0.75	2.10	151	13	258	19
1.00	2.26	201	2	199	3

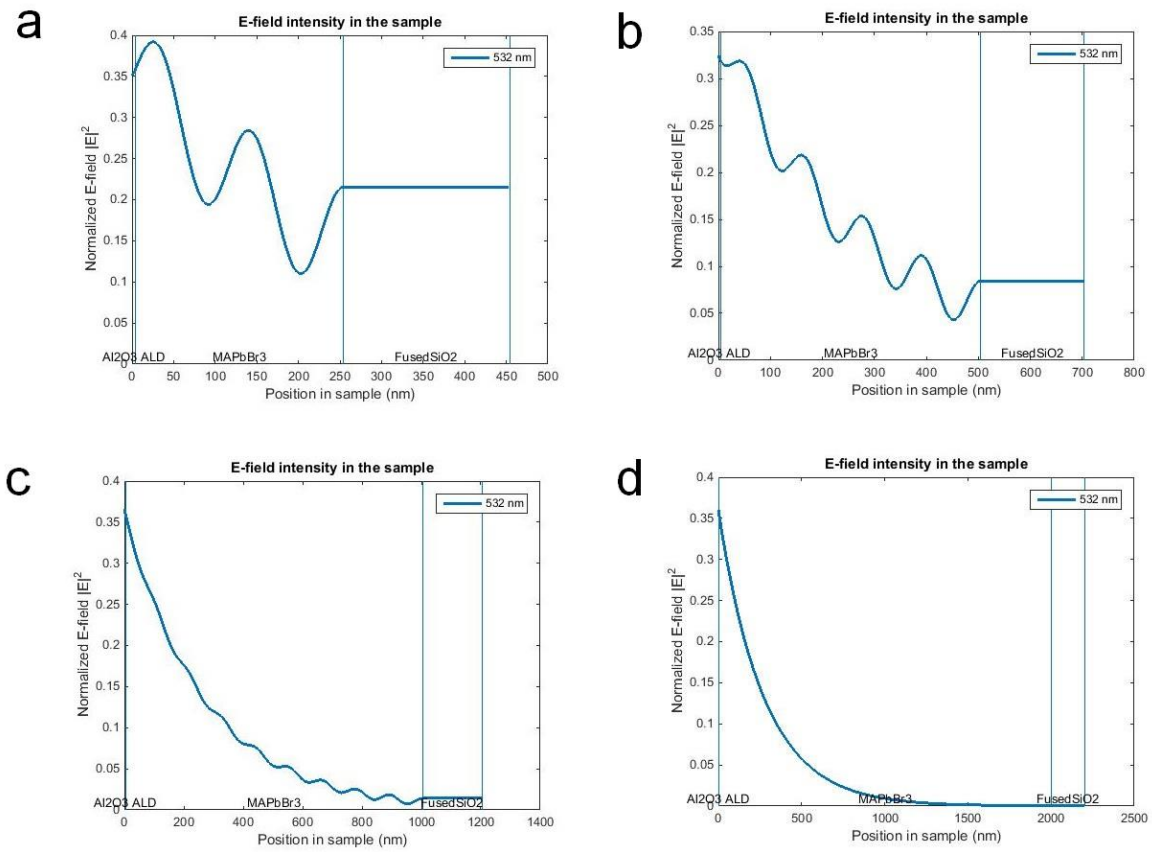

Figure S5. Electric field profile in $MAPbBr_3$ samples: The laser propagates from the left to the right side (air-Al_2O_3 ALD-$MAPbBr_3$-FusedSiO_2 interfaces). The thickness of $MAPbBr_3$ films vary from (a) 250 nm, (b) 500 nm, (c) 1000 nm, (d) 2000 nm.

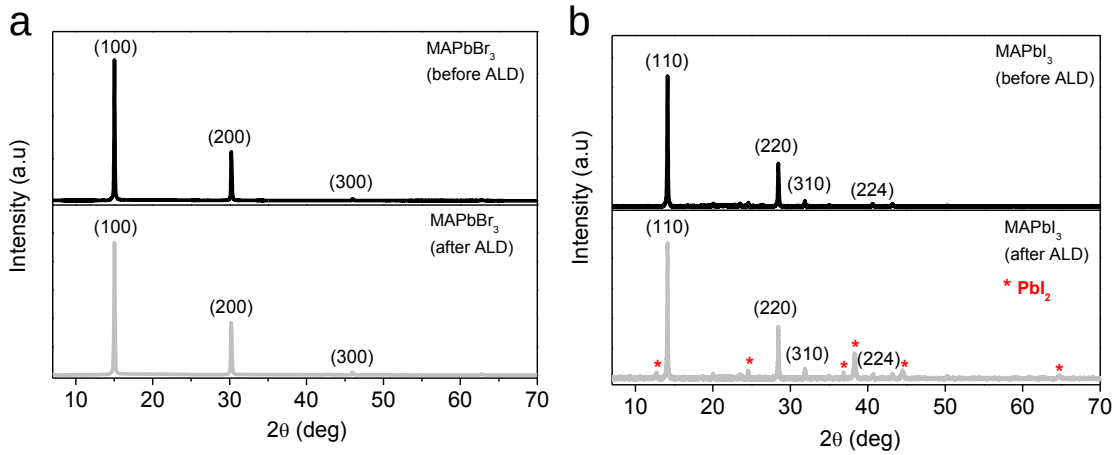

Figure S6. X-ray diffraction after ALD passivation.

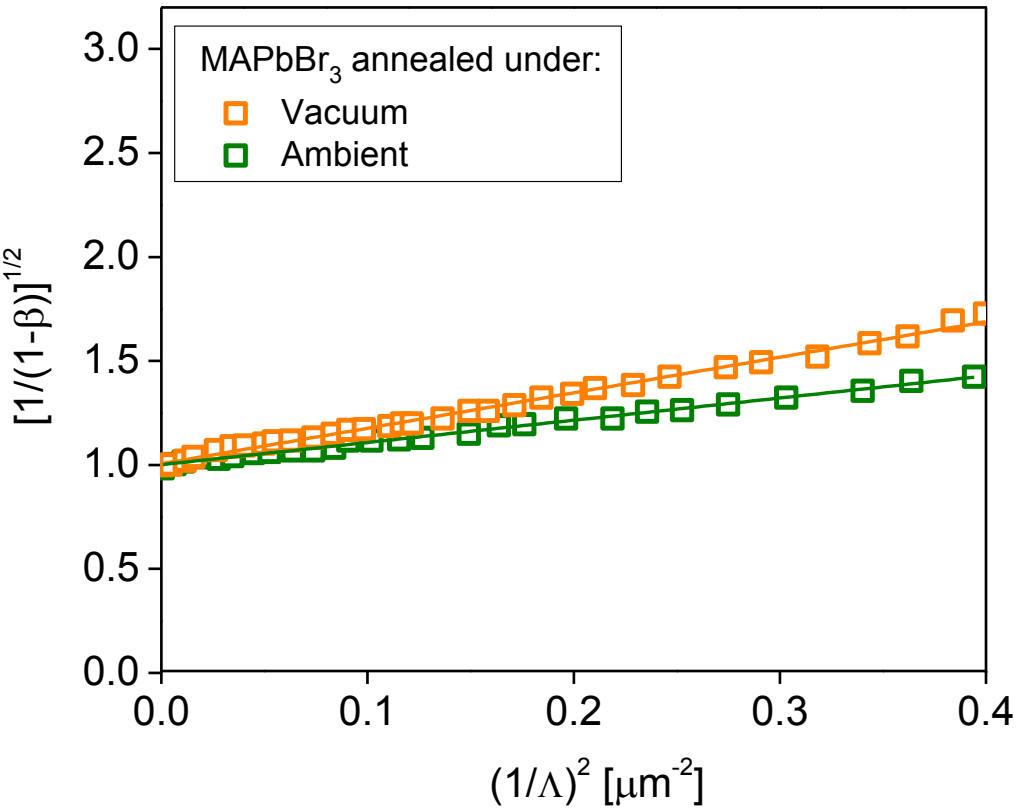

Figure S7. Diffusion length of $MAPbBr_3$ under different annealing.

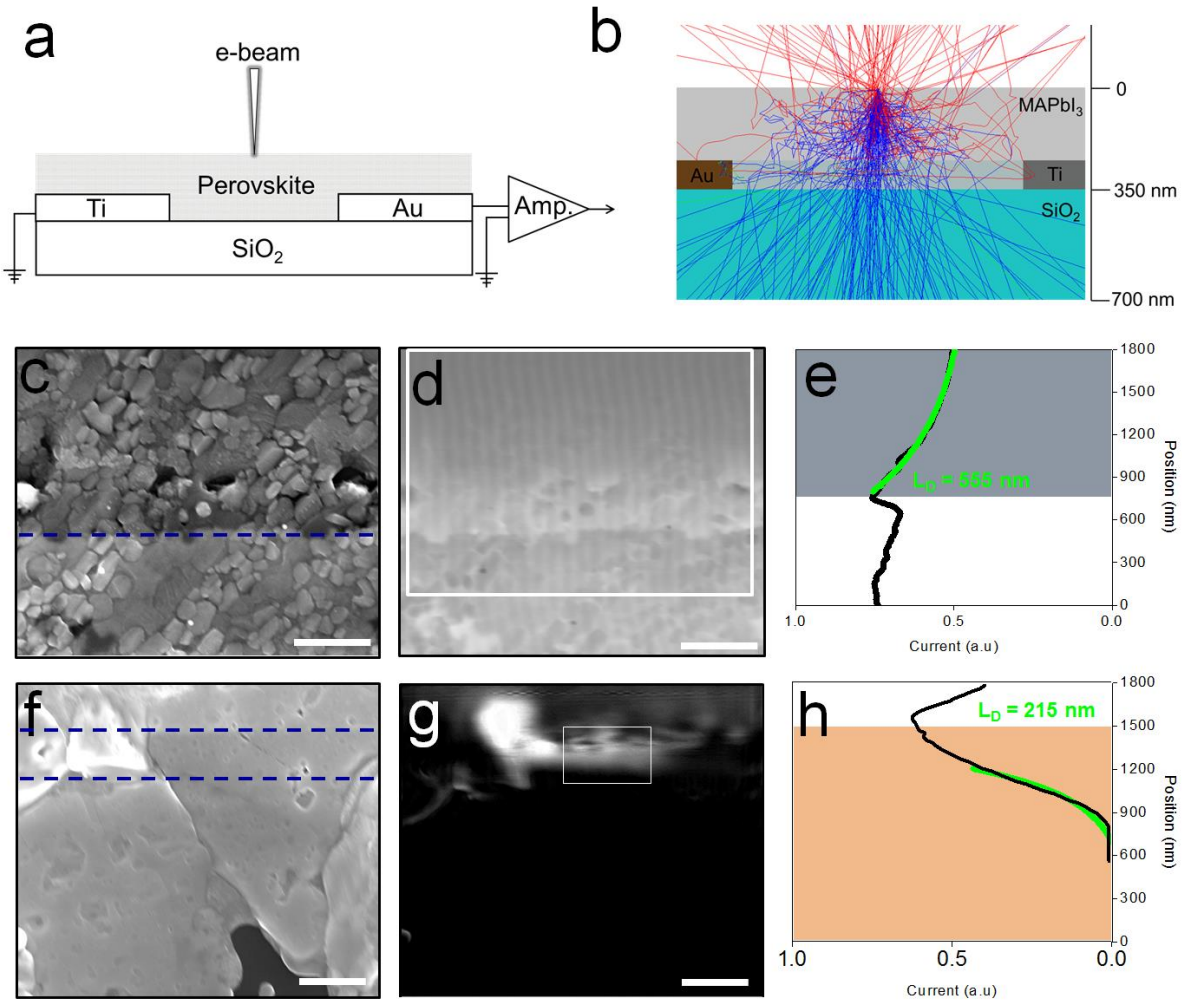

Figure S8. Electron beam induced current (EBIC) on $MAPbI_3$ and $MAPbBr_3$ films: (a) Measurement geometry. (b) Simulated electron trajectories and scattering events of the corresponding geometry in figure S8a (blue: secondary electron path; red: back-scattered electron path). (c) SEM image showing $MAPbI_3$ films on top of Au (bottom side; below the blue dashed-line) and Ti (beyond the top of the frame) contacts. (d) Corresponding EBIC image of figure S8c: darker areas indicate lower current; the scale bar for figure S8c-d is 400 nm. (e) Averaged current response profile from the EBIC extracted from figure S8d (framed with white line) showing an exponential decay tail toward the Ti side (gray area) of the depletion region (the green line is the fitting curve from which the diffusion length is obtained; L_D = 555 nm). (f) SEM image showing $MAPbBr_3$ films on top of Au (bottom side; below the bottom blue dashed-line) and Ti (top side; above the top blue dashed-line) contacts. (g) Corresponding EBIC image of figure S8f: darker areas indicated lower current; the scale bar for figure S8f-g is 2 micron. (h) Averaged current response profile from the EBIC extracted from figure S8g (framed with white line) showing an exponential decay tail toward the Au side (orange area) of the depletion region (the green line is the fitting curve from which the diffusion length is obtained; L_D = 215 nm).